Numerical modelling of the morphological change in Lhok Nga, west Banda Aceh, during the 2004 Indian Ocean tsunami: understanding tsunami deposits using a forward modelling method

Linlin Li[1] · Qiang Qiu[1] · Zhenhua Huang[1,2]

[1]*Earth Observatory of Singapore, Nanyang Technological University, Singapore*

[2]*School of Civil and Environmental Engineering, Nanyang Technological University, N2-01a-05, 50 Nanyang Avenue, 639798, Singapore*

Corresponding author e-mail: zhhuang@ntu.edu.sg (Zhenhua Huang)

Tel: +65 67904737

Abstract A coupled hydrodynamic and morph-dynamic model COMCOT-SED was used to investigate the morphological change in Lhok Nga bay during the 2004 Indian Ocean tsunami, and the coupled model predicted the thickness of tsunami deposits in agreement with the measured ones. The relationship between characteristics of tsunami deposit and flow hydrodynamics was discussed in details. Phenomena such as landward thinning in deposit thickness, landward fining in grain size and fining-upwards in grain size are commonly used to identify tsunami deposits, and were examined in this case study. We also discussed the effects of sediment supplies and the constraints that can be put on the earthquake parameters using the information derived from tsunami deposits. This study shows that the model presented in this paper is capable of simulating extreme tsunami events (tsunami wave height~30 m) in a large domain and that forward models of tsunami sediment transport can be a promising tool to help tsunami geologists understand tsunami deposits.

Keywords *tsunami deposit · sediment transport · morphological change · tsunami hazards*

1 Introduction

Large tsunami waves can cause widespread and dramatic changes in coastal morphology by the erosion, transport and deposition of sediment during tsunami runup and backwash periods. The resultant tsunami deposits caused by modern tsunamis provide excellent opportunities to study the physical processes of tsunami inundation and sediment transport. Tsunami geologists have made significant effort to reconstruct the characteristics of tsunami flow (number of waves, flow depth and velocity) by establishing qualitative relationships between tsunami deposits and tsunami hydrodynamic characteristics (Jaffe and Gelfenbuam 2007; Moore et al. 2007; Morton et al. 2008; Spiske et al. 2010). This information can make it possible to interpret palaeo-tsunami deposits, aid in assessing the tsunami source locations and further allow us to estimate the recurrence intervals of past tsunamis (Martin et al. 2008; Nelson et al. 2006; Pinegina et al. 2003). However, the inverse modeling faces great challenges since tsunami deposits are highly variable and affected by local conditions such as tsunami wave form, coastal morphology, inland topography, sediment composition and availability. These variations make the analysis of tsunami deposits equivocal and even contradictory sometimes because wave information is mostly derived from the spatial distribution and composition of the limited deposition sand samples (Clague et al. 2000; Dawson and Shi 2000; Moore et al. 2007; Smith et al. 2007; Switzer and Jones 2008; Martin et al. 2008; Pritchard and Dickinson 2008). To solve these problems, forward models of tsunami-induced sediment transport might be a promising method which could provide information on the time-varying flows and sediment transport in a straight forward way.

Currently, all the widely used tsunami simulation models, including MOST (Titov and Synolakis 1998), TUNAMI N2 (Goto et al. 1998) and COMCOT (Liu et al. 1995;

Wang 2009), have not considered the sediment movement when the tsunami waves propagate into nearshore areas and eventually flood low-lying coastal areas. However, large amounts of sediment from nearshore and onshore areas can be suspended and transported by the high-velocity tsunami waves which were observed by many tsunami witnesses and survivors as black water or turbid flows (Lavigne et al. 2009; Bourgeois 2009). Some numerical models have been developed to investigate the tsunami-induced sediment movement (Simpson and Castelltort 2006; Xiao et al. 2010; Sugawara et al. 2004; Takahashi et al. 2000; Goto and Imamura 2007; Apotsos et al. 2011a; Apotsos et al. 2011b; Nakamura et al. 2009). Most of them have only been validated using laboratory experiments, though some models have been employed to simulate the real-scale tsunami events, with the results in a qualitative agreement with the measured ones (Kihara and Matsuyama 2010; Apotsos et al. 2011a; Apotsos et al. 2011b). The following issues were encountered in the previous studies: 1) Most of these models cannot handle mixed grain sizes, resulting in low accuracy in the simulated sediment transport in view of the wide range of grain sizes involved (Goto and Imamura 2007); 2) Since sediment transport models can only be used in a small domain, conditions on the offshore artificial boundaries are usually provided by the results from another large-domain wave-propagation model (Apotsos et al. 2011a), but these artificial boundaries might cause unrealistic wave reflection (Apotsos et al. 2011a; Apotsos et al. 2011b); 3) The application of these existing models was limited to the moderate or small tsunami waves with the wave heights less than 5-10 m. It left us totally ignorant of large tsunami waves with a height larger than 15 m (or even 30 m). In view of the possibility that the tsunami deposits can be preserved in these more extreme situations, it seems particularly important to investigate relationships between characteristics of tsunami deposits and flow patterns under large tsunami waves.

By using a forward numerical model to examine the morphological changes, this study tries to interpret the tsunami deposits in Lhok Nga (on the west coast of Banda

Aceh) during the 2004 Indian Ocean tsunami. Some of the criteria commonly used to identify tsunami deposits will be examined through the forward method, including one or more layers of sediment that fine upward (grain size gets smaller toward the top of the layer), landward thinning in deposit thickness and landward fining in grain size. Relationships between the characteristics of tsunami deposits and flow patterns will also be discussed in detail. A two-way coupled model COMCOT-SED is developed, which is capable of simulating tsunami generation, propagation, inundation and morphological changes in a seamless way. Multiple sand layers and fractions are used to record the spatial and temporal changes of sand fraction in each sand layer. The coupled model is described in Section 2. The study area and the model setup are described in Section 3. The results and discussion are presented in Section 4, and main conclusions are summarized in Section 5.

2 Coupled Hydrodynamic and Morph-dynamic Model

The coupled hydrodynamic and morph-dynamic model is developed based on two open source codes: COMCOT and XBeach. COMCOT (COrnell Multi-grid COupled Tsunami Model) is capable of calculating the tsunami propagation in deep oceans and the inundation in coastal zones simultaneously. To balance the efficiency and accuracy, a nested grid system is adopted in which linear/nonlinear shallow water equations are solved on each grid layer using a modified leap-frog finite difference method. The reliability and accuracy of COMCOT have been proved through many applications, for example the 1992 Flores Islands (Indonesia) tsunami, the 2003 Algeria Tsunami and the 2004 Indian Ocean tsunami (Wang and Liu 2006). XBeach is a 2DH numerical model that can seamlessly simulate wave propagation, inundation, sediment transport and morphological changes (including dune erosion, overwash and breaching) under various wave and flow conditions. A detailed description of XBeach can be found in Reolvink et

al. (2009). The model has been tested with several analytical solutions, large-scale laboratory experiments, and several field observations (Deltares 2010; McCall et al. 2010; Roelvink et al. 2009; Li et al. 2011). However, XBeach can only be used for small areas due to its high demand on computer resources for high spatial resolution. To simulate both the flow field and sediment transport with high efficiency and accuracy simultaneously, we incorporated the sediment transport module in XBeach into the inner most grid layer of COMCOT, and the coupled model is named as COMCOT-SED. A two-way coupling of these two models is achieved in COMCOT-SED, which is capable of simulating the entire lifespan of a tsunami, from its generation, propagation, inundation on coastal regions, to the resulting morphological changes.

2.1 Two-way coupling algorithm

The two-way coupling algorithm used in COMCOT-SED is the same as that used in COMCOT, the reader can refer to COMCOT V1.7 manual (Wang 2009) for details. In COMCOT-SED, the nonlinear shallow water equations used in the innermost layer of COMCOT are replaced by those used in XBeach. Information on volume fluxes and free surface displacements is exchanged on the boundaries between two nested grid regions. At each new time level, the volume fluxes on the boundary of a finer grid are obtained by linearly interpolating, both spatially and temporally, the volume fluxes obtained from its outer parent grid; At each next time level for the outer parent grid, the free surface displacements on a coarser grid are updated by averaging, both spatially and temporally, the surface displacements obtained on the inner finer grid. To minimize the effect of sudden change in the bed elevation joining the innermost layer with its outer parent layer, a buffer area is introduced as a transitional region to interpolate linearly the change of the bed elevation across the buffer layer.

2.2 Shallow water equations

To simulate the tsunami wave propagation in deep oceans, linear shallow water equations are solved in a spherical coordinate system and the effects of the Coriolis force are included; To simulate tsunami-wave propagation near-shore and inundation onshore, the following depth-averaged nonlinear shallow-water equations are used (See Wang (2009) for details):

$$\frac{\partial \eta}{\partial t}+\frac{\partial hu}{\partial x}+\frac{\partial hv}{\partial y}=0 \qquad (1)$$

$$\frac{\partial u}{\partial t}+u\frac{\partial u}{\partial x}+v\frac{\partial u}{\partial y}+\frac{gn^2}{h^{4/3}}u\sqrt{u^2+v^2}=-g\frac{\partial \eta}{\partial x} \qquad (2)$$

$$\frac{\partial v}{\partial t}+u\frac{\partial v}{\partial x}+v\frac{\partial v}{\partial y}+\frac{gn^2}{h^{4/3}}v\sqrt{u^2+v^2}=-g\frac{\partial \eta}{\partial y} \qquad (3)$$

where η is the surface elevation; h is the total water depth; u, v are the depth-averaged velocities in the x- and y- directions, respectively; ρ is the water density; g is the gravitational acceleration; n is the Manning's coefficient for bottom roughness, which may vary spatially due to different land uses in the study area.

2.3 Sediment transport and morphological change

The sediment transport model is activated only on the innermost grid. The sediment movement is simulated by the depth-averaged advection-diffusion equation with a source term formulated by an equilibrium sediment concentration (Galappatti and Vreugdenhil 1985):

$$\frac{\partial hC}{\partial t}+\frac{\partial hCu}{\partial x}+\frac{\partial hCv}{\partial y}+\frac{\partial}{\partial x}\left[D_h h\frac{\partial C}{\partial x}\right]+\frac{\partial}{\partial y}\left[D_h h\frac{\partial C}{\partial y}\right]=\frac{hC_{eq}-hC}{T_s} \qquad (4)$$

where C is the depth-averaged concentration of suspended sediment; D_h is the sediment diffusion coefficient; T_s is the adaptation time of sediment concentration, given by the following simple approximation

$$T_s = \max\left(f_{Ts} \frac{h}{w_s}, 0.2 \right) s \tag{5}$$

which depends on the local water depth h, sediment fall velocity is w_s and a sediment transport depth factor f_{Ts} (default value is 0.1). As T_s approaches zero, the sediment concentration responses to the change of flow instantaneously. Both the entrainment and deposition of sediment are determined by the mismatch between the actual sediment concentration C and the equilibrium concentration C_{eq}. In this study, C_{eq} is calculated using the formula proposed by Van Rijn (1993) and the formulas for C_{eq} and w_s can be found in the manual of XBeach (Roelvink et al. 2008).

The bottom elevation z_b changes with time, and the change of bottom elevation is updated by the following equation

$$(1-p)\frac{\partial z_b}{\partial t} + \frac{\partial S_x}{\partial x} + \frac{\partial S_y}{\partial y} = 0 \tag{6}$$

where p is the porosity of bed material, and the sediment transport rates in *x*- and *y*-directions, S_x and S_y respectively, are given by

$$S_x = \frac{\partial hCu}{\partial x} + \frac{\partial}{\partial x}\left[D_h h \frac{\partial C}{\partial x} \right] \tag{7}$$

and

$$S_y = \frac{\partial hCv}{\partial y} + \frac{\partial}{\partial y}\left[D_h h \frac{\partial C}{\partial y} \right] \tag{8}$$

In our coupled model, up to 20 sand layers, which can be composed of multiple sediment classes, can be simulated by assigning different grain sizes for different areas (Fig. 1). These features allow us to record the change of fractional composition of each layer at each time step, and make it possible to establish relationships between tsunami deposits and tsunami flows. It is usually assumed that the top-layer is readily available for sediment pick-up. To simulate the multiple sand classes in multiple-layers, the coupled model adopts the procedures described below. For each sediment class, the equilibrium sediment concentration is calculated according to the Van Rijn's formula (1993). From the fraction of the *i*-th sediment class in the top-layer $frc(i,1)$, the equilibrium concentration $C_{eq}(i)$ used in Eq. (4) for the *i*-th sediment class can be calculated by

$C_{eq}(i) = frc(i,1)C^*_{eq}(i)$, where $C^*_{eq}(i)$ is the equilibrium sediment concentration for the *i*-th sediment class under the assumption that the bed is consisted of sand with a single diameter of same as the diameter of the *i*-th sediment class. Using Eq. (4), the concentration of suspended sediment is calculated independently for each sediment class to give its sediment transport rate. The bed elevation caused by the *i*-th sediment class is then updated using Eq. (6) with the known sediment transport rate for this sediment class. The total change of bed elevation is the sum of the changes caused by all sediment classes. The fraction of each sediment class in the top layer, $frc(i,1)$, can be calculated according to the relative ratio of the bed-elevation change caused by each sediment class, the total bed elevation change and the thickness of the top layer.

3 Study area and model setup

3.1 Study area

Lhok Nga Bay is located 13 km southwest of Banda Aceh, Northern Sumatra (Fig. 2), which is the area most severely affected by the 2004 Indian Ocean Tsunami. The maximum tsunami height was more than 30 m, with a maximum runup height of about 51 m. This ranks as the highest runup value measured in human history for a seismically generated tsunami (Lavigne et al. 2009). Since it is an extremely infrequent and catastrophic event, Lhok Nga has been well investigated, with all kinds of valuable data measured and collected during several post-tsunami field surveys (Borrero 2005; Jaffe et al. 2006; Meilianda et al. 2010; Paris et al. 2010; Paris et al. 2009; Lavigne et al. 2009). A comprehensive database for this area was provided by Lavigne et al (2009). This database includes detailed topographic and bathymetric datasets, tsunami heights, inundation distances and tsunami deposit thicknesses. These data allow us to test our numerical models in a full scale setting.

3.2 Fault model for 2004 Sumatra-Andaman earthquake

The characteristics of the great Sumatra-Andaman earthquake of 2004 were only partially understood due to its exceptionally complex nature. Data sets collected from different sources (seismic waves, far and near-field GPS data, remote sensing measurements of uplift or subsidence using optical or Synthetic Aperture Radar (SAR) images, tide gauges and satellite altimetry measurements) have been used to invert for fault geometry, coseismic slip distribution and rupture process of this event (Ammon et al. 2005; Banerjee et al. 2007; Bilek 2007; Chlieh et al. 2007; Fujii and Satake 2007; Piatanesi and Lorito 2007). Most of the available fault plane models have been inverted just using part of the aforementioned information (such as only seismic waves or far-field GPS data). Few models have reconciled the tsunamigenic source, the seismological data and the geodetic data. In this study, we chose one of these few fault models proposed by Banerjee et al (2007) (updated by Piatanesi and Lorito (2007)). The model from Banerjee et al (2007) was updated by Piatanesi and Lorito (2007), who further constrained the source parameters using 14 tide gauge records. To generate the tsunami, Okada's model (1985) was used to calculate the seafloor displacement, with the initial surface elevation following the sea floor deformation instantaneously. The initial sea surface elevation map corresponding to the rapture model used in this study is given in Fig. 3. Wang and Liu (2006) pointed out that no significant quantitative differences existed between the inundation predicted by an impulsive fault model and its corresponding transient model, therefore, the rupture process is not considered in this study.

3.3 Bathymetry and topography

The setup of computational grids is shown in Fig. 4. Five nested grids (Grid 01~ Grid 05) were used, with the grid resolution varying from 1944 m in the source region to 18 m in the city area (see Table 1). In the deep-ocean area, we used a 30 arc-second grid

(ca. 925m) from the GEBCO digital bathymetry/topography data set to create the computational grids for Grid 01~ Grid 03. Pre-event data of 70-m resolution was used for Grid 04 covering the nearshore and land areas, and pre-event data of 18-m resolution was used for Grid 05 covering the west coast of Lhok Nga (downloaded from www.tsunarisque.cnrs.fr/bd_tsuna.htm). The pre-event data was constructed by the TSUNARIQUE research team based on the data from various sources. The topographic data was derived from the following sources: a) extensive field topographic data measured one month after the event; b) Banda Aceh topographic maps with scales of 1:2000 and 1:5000 and the Lhok-Nga topographic map with a scale of 1:10000; c) SRTM DEM (90 m). The bathymetric data was derived from the following sources: i) the continental shelf bathymetric data measured through several echo sounding campaigns using GPS echo sounders; ii) NorthWest Sumatra bathymetric map (with a scale of 1:100000, Sheet Sumatera Pantai Barat Laut dan Pulau-Pulau Sekitarnia, 2001); iii) Global GEBCO Digital Atlas. To reconstruct the pre-event topography data, high-resolution satellite images for Banda Aceh and Lhok Nga from IKONOS (CRISP 2004) before and after the event were compared. The information was also complemented by non-eroded markers such as soil surface, roads, roots and the remaining of ante-tsunami sand dunes, and the interviews with local inhabitants. The details of the five nested grids used in this study are summarized in Table 1.

3.4 Map of roughness coefficient

In this study, bed roughness was parameterized using a Manning's roughness coefficient, n, which varied spatially according to different land uses/covers (see Fig. 5).

We classified the innermost layer into six type of areas based on the geo-referenced high-resolution satellite image IKonos (CRISP 2004) in Lhok Nga: forest areas, beach areas, vegetation areas, agriculture areas, settlements and water areas. For each area, a different Manning's coefficient was specified according to the guide for selecting the Manning's

coefficients for natural channels and floodplains (Arcement and Schneider 1989). A constant value of 0.013 was specified for the water areas. For the densely populated settlement areas, city buildings would dissipate more tsunami wave energy locally (Huang et al. 2009; Qiu et al. 2010), so a high roughness value was given ($n = 0.06$). Similarly, higher roughness values were specified for the densely forest areas ($n = 0.035 \sim 0.04$). Practically, the bed roughness likely varies temporally as well when the covered vegetation is uprooted and sediment is deposited. However, this effect is not considered in this study.

3.5 Initial sand distribution and composition

According to post-tsunami field surveys, Lhok Nga experienced severe geomorphologic changes, evidenced by distinct erosion imprints extending to 500 m landward from the shoreline (2 km inland along the river beds). Almost all the buildings and trees were swept away. The vegetation cover was totally stripped off, exposing the barren sand/soil and intensifying the erosion process (Meilianda et al. 2010; Paris et al. 2007; Paris et al. 2009). The beach area consists of fine sand with the grain size D_{50} being in the range of 0.14~0.25 mm. The sand samples collected in this area revealed that most of the tsunami deposits were composed of medium and coarse sand with the particle size within the range of 0.23~0.8 mm (Paris et al. 2007). Based on this information, two well-mixed sand classes with grain sizes of 0.2 mm (50%) and 0.8 mm (50%) were specified in the entire simulation domain. The thickness of the erodible bed was assumed to be unlimited, i.e., there is an adequate supply of sediment in the simulated area. We specified 20 layers with a uniform 3-cm thickness for each layer to record the change of fractional composition in each layer. In this study, we did not consider the effect of vegetation.

4 Results and discussion

4.1 Tsunami heights and inundation in Lhok Nga

Fig. 6 shows the simulated inundation map and a comparison of the surveyed tsunami heights and those computed using the source model of Banerjee et al (2007). Basically, the model predicted severe flooding in Lhok Nga and all the low-lying areas were submerged except some small highlands with the elevation in the order of 20 m. The simulated inundation map is similar to the one surveyed by TSUNARISQUE research group (see Fig. 3 in Lavigne et al., (2009)). From the comparison between the simulated tsunami heights and the field data collected by the same research group (Lavigne et al. 2009), it was found that the fault model generated tsunami waves heights in the order of 20 m and the simulated results matched reasonably well with the measured ones. At some locations, the tsunami heights were underestimated by 23% on average. The underestimation of tsunami heights is quite normal when a fault model derived from a seismic inversion or GPS information is directly used without amplification (Geist 2002). Actually, our simulated tsunami heights show much better agreement with the measured ones than previous studies (Wang and Liu 2007; Wijetunge et al. 2008).

4.2 The relationship between flow characteristics and sediment transport process

Fig. 7 shows the process of the simulated tsunami flooding and the corresponding morphologic changes through snapshots of velocity distribution and bed elevation at several typical instants. The first wave front reached the west coast of Lhok Nga about 21 minutes after the rupture, with the flow velocity on the order of 20 m/s. The leading wave moved rapidly landward, with the flow depth ranging from 0.5 m to 5 m and carrying large amounts of sediment. The area close to the shoreline was eroded by the passing wave front and deposition occurred when the wave front passed by. Just 6 minutes later, the direction of the flow close to the shoreline began to change to the seaward direction

before the wave front reached the inundation limit. A portion of the sediment entrained by the wave front was deposited first and then immediately eroded by the subsequent passing waves (see Fig. 7 (b2)). Fig. 7 (c2) shows that large areas close to the shoreline were subject to erosion and seaward transport of sediment. As shown in Fig. 7(d1) and Fig. 7(e1), the velocity of backwash flow was greatly influenced by the nature of the local coastal topography, and strong backwash flow concentrated in the topographic lows and speeded up by the steep slopes on the flow path. Within the first hour of wave attack, significant sediment transport occurred near the shoreline during the backwash period, resulting in a net erosion of the shore face. Much of the eroded sand was transported off-shore to the active coastal zone by the backwash flow, resulting in a maximum deposition depth of 3.0 m in the bay area (see Fig. 7(g2)). This phenomenon is consistent with the bathymetric surveys conducted after the 2004 tsunami at Kuala Meurisi (a site about 100 km south of Banda Aceh), where a large offshore bar was observed (Gelfenbaum et al. 2007). After the first wave, three more waves flooded this area, but the morphology did not undergo much change.

Since the measured thicknesses of tsunami deposit are normally in the order of several centimeters or tens of centimeters, it is difficult to identify the difference from the planar figures. Fig. 8 gives the time series of the free-surface elevations and the bed-elevation changes at four selected locations in the first 3 hours. At LOC-3, located in a low area 300 m from the shoreline, tsunami deposits with a thickness of about 1.5 cm were left after the first wave peak (12 m), but the deposits, together with local sand, were then totally eroded away by the following backwash flow. The backwash flow of the first wave encountered the uprush flow of the second small wave that slowed down the erosion speed. After the first two waves, but before the third wave arrived, the water stored in the low-lying rice field began to drain out towards the sea, causing additional erosion and sediment re-deposition. The third wave came around 80 min after the rupture and brought about 4-cm thick sediment deposits, but the following backwash flow eroded

sediment thicker than 4-cm, resulting in a measureable erosion at LOC-3. Similar processes also happened during the successive waves but the morphology was only slightly changed since the wave heights were much smaller than the previous ones. In this location, no deposit was left since the erosion dominated the repetition of this deposition-erosion process. At LOC-6, similar processes were observed in which the uprush flow deposited sediment and backwash flow eroded the previous deposition. However, an exception occurred between 50 min and 80 min; deposition happened during the backwash period after the deepest erosion depth was reached. It may be because the backwash flow has a slow velocity from which sediment can be easily settled out; it may also because that the tsunami waves reach zero velocity before the backwash flow begins, and a large volume of sediment can be deposited out of the water column onto the ground surface during this period. LOC-11 is located in the further inland area where the tsunami waves gradually lose their energy, with the maximum heights less than 8 m. The flooding water maintains a relative stable flow depth indicating that the water is almost stagnant in this area, resulting in only slight elevation changes after the first wave. LOC-19 lies in the southern part of the coast, about 400 m from the shoreline. The inundation line did not exceed 400 m due to the steep topography. The deposition-erosion process was repetitive during the subsequent waves and the magnitudes of erosion depth and deposit thickness were relatively small compared with the ones at LOC-1 through LOC-5, probably because a small amount of water flooded onshore and did not cause significant sediment movement in this area.

According to our analysis, we found that several scenarios could be present if one particular location experienced multiple waves: 1) Successive tsunami waves may remove the pre-existing tsunami deposit, especially in the topographic lows where strong backwash flows concentrate. Dawson and Shi (2000) believed that one of the last waves within a tsunami wave train could be capable of eroding most of the sediment deposited by the preceding waves. If all the deposits brought by each previous wave are eroded by

the following one, then no deposit can be found after the event. This scenario was found at LOC-3; 2) Each successive tsunami wave just erodes part of the pre-existing tsunami deposit, i.e., there is some amount of deposits can be left after each wave. 3) Some of the tsunami deposits left by the previous wave are partly eroded while others are totally removed. A frequently asked question is whether the vertical grain size distribution in tsunami deposits can provide information on the approximate number of waves during a tsunami event. To answer this question, we marked the thickness of the sand layers left by each successive tsunami wave at 4 locations. At LOC-6, LOC-11 and LOC-19, the tsunami deposits were divided into 3 different parts that were formed by three main waves. Assuming that coarser sand settles out of suspension before finer sand, these different parts can be identified as fining upward sequences which have been observed in most of the modern tsunami deposits. In this regard, we may say that tsunami deposits have the potential to record the number of tsunami waves they have experienced. We notice that the minimum thickness of these sand layers is less than 0.3 cm, which may not be easily identified in field surveys if large intervals of sand samples are taken. Sampling intervals, as used by most tsunami geologists, are normally in the order of 1-cm or 2-cm, therefore, the details of the sedimentary record may be missed from the surveyed results. If the vertical textural variability is at the millimeter scale, broader sampling may lead to different interpretation (Morton et al. 2008)

It needs to be stressed here that the tsunami deposit thickness measured by geologists after an event only record the final stage at that particular location; therefore, we cannot simply use the difference between pre- and post- event topographical data (after removing the bed-elevation change due to the subsidence caused by the earthquake) as a criteria to determine whether the location has the tsunami deposit or not. Practically, the local tsunami-deposit thickness is the difference between the final bed elevation and the lowest eroded base. Fig. 9 gives a comparison of the simulated deposit thickness with the measured one, showing that the model can give a reasonable prediction of the

deposition thickness. From LOC1 to LOC14 along the profile A-A, the simulated tsunami deposit thicknesses show the same trend as the measured one. In view of the complex local topography and the uncertainty in the initial model setup, the simulated results are acceptable and other valuable information about the processes occurring during a tsunami event can be provided by numerical simulations.

4.3 The spatial distribution and characteristics of tsunami deposits

To investigate the spatial distribution of tsunami deposits, we extracted the information on topography, maximum inundation depth, thickness of the tsunami deposits, the vertical equivalent particle sizes at typical locations and the lateral equivalent particle sizes along the two transects A-A and B-B (Fig. 10, see also the cross-sections A-A and B-B in Fig. 2). The orientations of these two cross-sections were chosen to follow the main directions of the tsunami flows. The topography along the cross-section A-A is relatively low and flat. The inundation depth was about of 15 m and slightly decreased in the inland areas. The deposit thicknesses ranged from 0 to 35 cm and an obvious landward thinning trend was observed, which is similar to the measured data. The maximum deposit thickness was observed in the low-lying area close to the shoreline. For the cross-section B-B, the topography is undulated with two small highlands blocking the tsunami flow. A general landward thinning of deposit thickness from 48 cm to 5 cm was observed. A clear relationship between the topography and the deposit thickness is demonstrated in Fig. 10. Similar to the cross-section A-A, the thick deposits were found in the topographic lows but none deposits in highs: 48-cm thick deposits in the low-lying area between two highlands but none on the top of the highland area. The distribution of tsunami-deposit thickness have been described by many published papers, which have suggested that the thickest deposits usually occur locally in low-lying areas or around obstructions (Peters et al. 2007; Moore et al. 2007; Smith et al. 2007; Morton et al. 2008). These characteristics suggest that good places for tsunami geologists to dig out the palaeotsunami deposits are in the coastal gullies and in front of steep cliffs.

Tsunami deposits reported in the literature typically show that several upward-fining sequences (a sequence is an isolated upward-fining segment in a sediment core sample) can be formed during a single tsunami event (Dawson and Shi 2000; Moore et al. 2007; Morton et al. 2007; Peters et al. 2007; Smith et al. 2007; Shi et al. 1995). Some authors have correlated the upward-fining sequences with individual waves (Smith et al. 2007). As we discussed in Section 4.2, tsunami deposits have the potential to record the number of tsunami waves they have experienced, providing that the intervals of sand samples used in a tsunami-deposit analysis are small enough. In our simulations, 20 sand layers with a uniform 3-cm interval were used (more sand layers with smaller intervals are not realistic since it already took 14 days for each case studied here). Along the cross-sections A-A and B-B, we extracted the equivalent grain size of each layer vertically at 5 locations, see Fig 10-c. Even though the deposition thicknesses were different at different locations, one single fining-upward sequence was always observed at each location. This phenomena explains the observations that one or more fining-upward sequences were found in some modern tsunami deposits and palaeo-tsunami deposits (Dawson and Shi 2000; Smith et al. 2007; Dawson et al. 1996; Moore et al. 2007; Shi et al. 1995). The reason why only one fining-upward sequence was found in this study is because only two sand classes and the large layer interval were used. This is a simplified model, since in practice a variety of grain sizes, ranging from silt to boulders, exist and can be transported by tsunami waves. Future work needs to be carried out on computer clusters in order to examine in more detail the effects of more sand classes and finer layer intervals.

Lateral grain-size distributions along the cross-sections A-A and B-B are shown in Fig. 10-d. Along the cross-section A-A, the grain size was fining landward with a thinning trend for the deposit thickness, which indicates that fine sand contributed to a large portion of the deposit. The grain-size trend at the cross-section B-B did not follow the landward fining feature and was determined mainly by the complex local topography. The correlation between the grain size and deposit thickness seems positive in most of the

examined locations even though local effects of the topography also play an important role. General landward fining trend was observed only in some post-tsunami field surveys. Usually, the trend of landward fining may be connected to the reduction in the transport capacity of tsunami waves moving inland. Tsunami waves gradually lose their energy when they surge onshore and the velocity (a measure of sediment carrying capacity) decreases while the flooding water moves inland. As a result, the coarser sediment contained in the uprushing flows settles out first, and finer sediment can be carried farther inland. It is not surprising if no general trend of landward fining can be found in some of the surveyed sections: even though the trend of landward fining can be formed by the first inundation wave, there is no guarantee this trend can be preserved after the reworking of each subsequent wave. Moreover, the interaction between complex topography and tsunami waves always contribute greatly to the unpredictable characteristics of tsunami deposits.

4.4 The role of sediment sources

It is difficult to identify the origins of tsunami deposits. Previous studies have found that the deposits can come from offshore areas in deep water, shallow shelf, beach area and overland area. Sato et al. (1995) found that the 1983 and 1993 tsunami deposits in Japan came mainly from beach areas. According to the composition of tsunami deposits found at three sites in eastern Scotland, deposited by the Holocene Storegga Slide tsunami, Smith et al. (2007) suggested that the sand deposits were likely derived from local sources. Similarly, Shi et al. (1995) found ample indications that the tsunami deposits left by the 1992 tsunami in Nebe, Flores, Indonesia were largely derived from local coastal soil.

However, marine sediment is still believed to be the main contributor to tsunami deposit in some surveyed areas; for example, Gelfenbaum and Jaffe (2003) estimated that as much as 2/3 of sand in the deposit originated from offshore during the 1998 tsunami in

Papua New Guinea. Therefore, the presence of marine sand is one of the indications used to indentify tsunami deposits.

To investigate the effects of the sediment sources, three more simulations were conducted with different initial sand distributions. Four initial sand distributions used in this study are listed in Table 2. The difference among these distributions lies in the sand grain-size composition and the erodibility of the onshore area. Fig. (11a)~ (11h) give the distributions of volume percentage of 0.2-mm sand in the topmost layer for each case at t=0 and one-hour after the tsunami attack. For the distribution DA, fine particles were transported farther inland than the coarser ones (see Fig. 11(e)). This is because small settling velocity makes the finer particles settle down slower than the coarser ones in same places, leaving the finer sand deposited in the upper layer and farther inland. Even though the fine sand particles from the deep offshore area (up to 30-m deep) could be suspended and transported by the strong tsunami waves, our simulations did not show significant change of the bed elevation in deep offshore area, which makes it impossible to draw any conclusion on the existence of offshore tsunami deposits. However, Weiss and Bahlburg (2006) pointed out that the seabed area with water depth greater than 65 m was more likely to preserve tsunami deposits even large storm surge could happen after that tsunami event. For the distribution DB, where the fine sand particles only existed in the offshore area, tsunami waves entrained a large amount of fine sand from the offshore area and deposited most of the fine sand particles in the further inland areas (Fig. 11(f)). It was found that about 59.5% of the deposited sand was from the offshore area. For the distribution DC, similar to what was observed for the distribution DA, mean sand size in the top layer was reduced after the sorting process occurred during the uprushing and backwash periods (see Fig. 11(g)). For the distribution DD, the erodible sediment existed only in the seaside areas, less fine sand was found in the top layer due to the limited sediment supply in the inland areas. The onland area close to the shoreline had no deposits, which may be explained by the high uprushing velocity and the strong

backwash flows in this area, leaving no chance for any possible deposition in non-erodible areas (Fig. 11(h)).

Fig. 12 shows a comparison of the simulated deposit thicknesses for sand distributions DA, DB, DC and DD with the measured data. It demonstrates that the thickness of tsunami deposits was affected by the composition and availability of sand. The distribution DC (with three well-mixed sand classes) predicted the thickest tsunami deposit and overestimation of deposit thickness was found at several locations. The distribution DB (with fine sand initially in the seabed) predicted the thinnest deposit, indicating that the content of fine sand distributed initially onshore may play an important role in determining the final thickness of deposited sand. Compared with the distributions DA, DB and DC, the deposit thickness predicted for the distribution DD was almost unnoticeable, which emphasizes the importance of sediment supply. Though different in the magnitude, the simulated results based on these four different initial sand distributions did follow the trend of the measured data. It means that the thickest deposition can always be found at LOC-5, which is close to the shoreline and the topography at this location is low. This finding suggests that onshore topography is a key parameter to influence the tsunami deposit distribution under the same hydrodynamic condition. The initial sand distribution can affect the magnitude of predicted deposit thickness, but the general trend of deposit thickness is mostly controlled by local topography.

4.5 The role of tsunami sources

The information provided by tsunami deposits (spatial distribution, thickness, grain size) is expected to have the potential to record flow characteristics, and can further constrain the location and nature of earthquake ruptures (Martin et al. 2008; Nelson et al. 2006; Bourgeois 2009). However, the complexity of earthquake mechanisms always makes this kind of inverse modeling susceptible. To investigate how much constraint can be put on the earthquake (magnitude, location) by using the information derived from

tsunami deposits, we conducted two more simulations based on the fault model of Chlieh et al (2007) with different magnitudes. The model of Chlieh et al (2007) is believed to have used the most comprehensive sets of geodetic data and have been proved to fit relatively well with the altimetric measurements made by the JASON and TOPEX satellites in the deep-sea area. The initial surface elevation maps for these three fault models are given in Fig. 3 (source model A) and Fig. 13 (source model B and source model C), the same initial sediment distribution was specified (a sand mixture of three sand classes with grain sizes of 0.2 mm, 0.5 mm and 0.8 mm in the entire simulation domain).

Compared with the measured tsunami heights in the west coast of Lhok Nga bay, three cases all underestimated the heights but with different degrees (Fig. 14a). Source model C gives the lowest tsunami heights with an average value of 10 m, which is within 1/3 and 1/2 of the measured data. The results given by the source model A are slightly lower than those given by the source model B. As shown in Figs. 14b~c, high tsunami waves generated thicker deposits while low waves gave less deposit. The positive correlation between tsunami heights and the resultant deposit-thickness suggests that the thickness of tsunami deposits may be indicative of tsunami-height magnitude, provided that sediment supply is unlimited. To further examine the relationship between tsunami heights and the nature of earthquakes, basic parameters for fault models, such as rupture length, width, location and magnitude of dislocation, were examined by comparing the tsunami heights generated. In general, three source models have almost the same rupture length (Fig. 3 and Fig. 13). For each source model, the rupture area in the offshore area of North Sumatra can be divided roughly into two main broken segments: Andaman-Nicobar segment and northern Sumatra segment. The northern tip broken segments in the source models B and C does not contribute to the inundation because of the small uplift in this area. Compared with the source modes B and C, the location given by the source model A had a north-eastern shift, which made the northern Sumatra segment much

closer to the coast of Lhok Nga, with a maximum uplift value around 5.5 m. The maximum uplift value of the northern Sumatra segment was also around 5.8 m for the source model B, which generated tsunami heights in Lhok Nga similar to the source model A, though much larger uplift and subsidence existed in the Andaman-Nicobar segment. The generated tsunami heights in Lhok Nga were controlled mainly by the uplift value of the northern Sumatra segment, which is close to the studied area. The exact location of the northern Sumatra segment and the magnitude of the far-field seafloor displacement had little influence on the resulting tsunami heights. Inversely, it means that the constraints put on the magnitude and location of tsunami source by the tsunami heights is limited to the near-field area. To further explain this in more detail, we take 2004 Sumatra-Andaman earthquake as an example. If one historic or pre-historic earthquake like 2004 Sumatra-Andaman earthquake needs to be reconstructed using the information provided by tsunami deposits, the datasets need to be collected not only from the west coast of North Sumatra but also from all the other coastal areas in the Indian Ocean. Based on the tsunami heights derived from tsunami deposits, the magnitude of necessary seafloor displacement may possibly be deduced. However, to further constrain the location and the internal structure of this earthquake, comprehensive information is needed, including available historical tsunami records, palaeo-tsunami records, seismological records of the Sunda trench, offshore geology and geophysical surveys.

5 Conclusions

A coupled hydrodynamic and morph-dynamic model COMCOT-SED was used to investigate the morphological change in Lhok Nga bay during the 2004 Indian Ocean tsunami. The two-way coupled model is capable of simulating the extreme tsunami event (tsunami wave height~30 m) in a large domain. The predicted thickness of tsunami deposits is of quantitative agreement with the surveyed data. Main conclusions are summarized as follows: 1) Deposition happens during both the uprushing and backwash

periods as well as the turnaround period in between. Tsunami deposits have the potential to record in the upward-fining sequence the number of waves they have experienced. 2) At the locations experiencing repetitive erosion and deposition, the tsunami-deposit thicknesses measured by geologists after an event record only the accumulated effects of flow on sediment deposits. Since it is not easy to re-construct the erosion depth or deposition thickness caused by each tsunami wave based on the final thickness of sediment deposits, tsunami heights that are deduced from the tsunami deposits by using inverse models can be significantly underestimated. 3) Local topography has very important effects on the characteristics and spatial distribution of tsunami deposits. The thickest tsunami deposits usually occur in topographic lows or around obstructions, which suggests that coastal gullies and the front areas of steep cliffs have more chances to trap and preserve tsunami deposits. 4) The thickness of tsunami deposits can be affected by the composition of initial sand distribution and the availability of sand. Much less deposit can be left after tsunami if the sediment supply is limited to just offshore regions. 5) The information provided by tsunami deposits (spatial distribution, thickness, grain size) can be used to constrain the possible seafloor displacement close to the tsunami deposit area. To further constrain the location and internal structure of a large earthquake such as the 2004 Sumatra-Andaman earthquake, information on tsunami deposits at multiple sites surrounding the ocean basin and comprehensive knowledge such as available historical tsunami records, the palaeo-tsunami records, seismological records of the investigated area, offshore geology and geophysical surveys are needed. In combination with data collected from post-tsunami surveys at multiple sites, forward modeling of tsunami-induced sediment transport can be a promising tool to enrich the information derived from tsunami deposits.

Acknowledgement

This work is supported by Earth Observatory of Singapore (EOS), Nanyang Technological University, Singapore, through the project “Tsunami Hazard Mitigation for West Sumatra”. Dr. Paramesh Banerjee, EOS, and Dr. Mohamed Chlieh of Université de Nice Sophia-Antipolis are acknowledged for providing the detailed parameters of their fault models. We would like to thank Dr. Ashar Lubis, EOS, for his help with the fault model selection. We are thankful to Dr. Emma Hill, EOS, for her proofreading and helpful suggestions on this paper. This is EOS contribution NO. 46.

References

Ammon CJ, Ji C, Thio HK, Robinson D, Ni S, Hjorleifsdottir V, Kanamori H, Lay T, Das S, Helmberger D, Ichinose G, Polet J, Wald D (2005) Rupture process of the 2004 Sumatra-Andaman earthquake. Sci 308 (5725):1133-1139

Apotsos A, Gelfenbaum G, Jaffe B (2011a) Process-based modeling of tsunami inundation and sediment transport. JGR 116:20. doi:doi:10.1029/2010JF001797

Apotsos A, Gelfenbaum G, Jaffe B, Watt S, Peck B, Buckley M, Stevens A (2011b) Tsunami inundation and sediment transport in a sediment-limited embayment on American Samoa. Earth-Sci Rev 107 (1-2):1-11. doi:10.1016/j.earscirev.2010.11.001

Arcement GJJ, Schneider VR (1989) Guide for Selecting Manning's Roughness Coefficient for Natural Channels and Floodplains. Water Supply Paper 2339. Washington D.C.

Banerjee P, Pollitz F, Nagarajan B, Bürgmann R (2007) Coseismic slip distributions of the 26 December 2004 Sumatra-Andaman and 28 March 2005 Nias earthquakes from GPS static offsets. Bulletin of the Seismological Society of America 97 (1 A SUPPL.):S86-S102

Bilek SL (2007) Using earthquake source durations along the Sumatra-Andaman subduction system to examine fault-zone variations. Bulletin of the Seismological Society of America 97 (1 A SUPPL.):S62-S70

Borrero JC (2005) Field data and satellite imagery of tsunami effects in Banda Aceh. Sci 308 (5728):1596

Bourgeois J (2009) Geologic effects and records of tsunamis. In: Bernard EN, Robinson AR (eds) The Sea: Tsunamis, vol 15. Harvard University Press, London, England, pp 53-91

Chlieh M, Avouac JP, Hjorleifsdottir V, Song TRA, Ji C, Sieh K, Sladen A, Hebert H, Prawirodirdjo L, Bock Y, Galetzka J (2007) Coseismic slip and afterslip of the great Mw 9.15 Sumatra-Andaman earthquake of 2004. Bulletin of the Seismological Society of America 97 (1 A SUPPL.):S152-S173

Clague JJ, Bobrowsky PT, Hutchinson I (2000) A review of geological records of large tsunamis at Vancouver Island, British Columbia, and implications for hazard. QSRv 19 (9):849-863

CRISP (2004) Center for Remote Imaging, Sensing and Processing. http://www.crisp.nus.edu.sg/tsunami/tsunami.html. Accessed 20 November 2011

Dawson AG, Shi S (2000) Tsunami deposits. PApGe 157 (6-8):875-897

Dawson AG, Shi S, Dawson S, Takahashi T, Shuto N (1996) Coastal sedimentation associated with the June 2nd and 3rd, 1994 Tsunami in Rajegwesi, Java. QSRv 15 (8-9):901-912

Deltares (2010) XBeach testbed report. Delft, The Netherlands

Fujii Y, Satake K (2007) Tsunami source of the 2004 Sumatra-Andaman earthquake inferred from tide gauge and satellite data. Bulletin of the Seismological Society of America 97 (1 A SUPPL.):S192-S207

Galappatti G, Vreugdenhil CB (1985) A depth-integrated model for suspended sediment transport. Journal of Hydraulic Research 23:359 - 377. doi:10.1080/00221688509499345

Geist EL (2002) Complex earthquake rupture and local tsunamis. Journal of Geophysical Research B: Solid Earth 107 (5)

Gelfenbaum G, Jaffe B (2003) Erosion and sedimentation from the 17 July, 1998 Papua New Guinea tsunami. PApGe 160 (10-11):1969-1999

Gelfenbaum G, Vatvani D, Jaffe B, Dekker F Tsunami inundation and sediment transport in vicinity of coastal mangrove forest. In: Proceedings of Coastal Sediments 2007, 2007. pp 1117-1128. doi:10.1061/40926(239)86

Goto C, Y.Ogawa, Shuto N, Imamura F (1998) Numerical method of tsunami simulation with the leap-frog scheme. IOC Manual, UNESCE. IUGG/IOC Time project, New York

Goto K, Imamura F (2007) Numerical models for sediment transport by tsunamis. The Quaternary Research 46 (6):463-475

Huang Z, Qiu Q, Sieh K, Megawati K, Natawidjaja DH, Wang X Numerical simulations of tsunami inundation for the city of Painan, Indonesia-- Effects of coastal vegetations and man-made structures In: In Proceedings of the 3rd South China Sea Tsunami Workshop, Penang, Malaysia, 2009.

Jaffe BE, Borrero JC, Prasetya GS, Peters R, McAdoo B, Gelfenbaum G, Morton R, Ruggiero P, Higman B, Dengler L, M.EERI RH, Kingsley E, Kongko W, Lukijanto, Moore A, Titov V, Yulianto E (2006) Northwest Sumatra and Offshore Islands Field Survey after the December 2004 Indian Ocean Tsunami. Earthquake Spectra 22:105-135

Jaffe BE, Gelfenbuam G (2007) A simple model for calculating tsunami flow speed from tsunami deposits. SedG 200 (3-4):347-361

Kihara N, Matsuyama M Three-dimensional hydrostatic numerical simulations on tsunami-induced sediment transport in a model harbor. In: The 3rd International Tsunami Field Symposium, Sendai, Japan, 2010.

Lavigne F, Paris R, Grancher D, Wassmer P, Brunstein D, Vautier F, Leone F, Flohic F, de Coster B, Gunawan T, Gomez C, Setiawan A, Cahyadi R, Fachrizal (2009) Reconstruction of tsunami inland propagation on December 26, 2004 in Banda Aceh, Indonesia, through field investigations. PApGe 166 (1-2):259-281

Li L, Huang Z, Qiu Q, Natawidjaja DH, Sieh K (2011) Tsunami-induced coastal change: scenario studies for Painan, West Sumatra, Indonesia. Earth, Planets and Space Article in press

Liu PLF, Yong-Sik C, Briggs MJ, Kanoglu U, Synolakis CE (1995) Runup of solitary waves on a circular island. JFM 302:259-285

Martin ME, Weiss R, Bourgeois J, Pinegina TK, Houston H, Titov VV (2008) Combining constraints from tsunami modeling and sedimentology to untangle the 1969 Ozernoi and 1971 Kamchatskii tsunamis. Geophys Res Lett 35 (1):L01610. doi:10.1029/2007gl032349

McCall RT, Van Thiel de Vries JSM, Plant NG, Van Dongeren AR, Roelvink JA, Thompson DM, Reniers AJHM (2010) Two-dimensional time dependent hurricane overwash and erosion modeling at Santa Rosa Island. Coastal Engineering 57 (7):668-683

Meilianda E, Dohmen-Janssen CM, Maathuis BHP, Hulscher SJMH, Mulder JPM (2010) Short-term morphological responses and developments of Banda Aceh coast, Sumatra Island, Indonesia after the tsunami on 26 December 2004. Mar Geol 275 (1-4):96-109

Moore AL, McAdoo BG, Ruffman A (2007) Landward fining from multiple sources in a sand sheet deposited by the 1929 Grand Banks tsunami, Newfoundland. SedG 200 (3-4):336-346

Morton RA, Gelfenbaum G, Jaffe BE (2007) Physical criteria for distinguishing sandy tsunami and storm deposits using modern examples. SedG 200 (3-4):184-207

Morton RA, Goff JR, Nichol SL (2008) Hydrodynamic implications of textural trends in sand deposits of the 2004 tsunami in Sri Lanka. SedG 207 (1-4):56-64

Nakamura T, Mizutani N, Yim SC (2009) A three-dimensional coupled fluid-sediment interaction model with bed-load/suspended-load transport for scour analysis around a fixed structure. Journal of Offshore Mechanics and Arctic Engineering 131 (3):1-9

Nelson AR, Kelsey HM, Witter RC (2006) Great earthquakes of variable magnitude at the Cascadia subduction zone. QuRes 65 (3):354-365

Okada Y (1985) Surface deformation due to shear and tensile faults in a half-space. Bull Seism Soc Am 75:1135-1154

Paris R, Fournier J, Poizot E, Etienne S, Morin J, Lavigne F, Wassmer P (2010) Boulder and fine sediment transport and deposition by the 2004 tsunami in Lhok Nga (western Banda Aceh, Sumatra, Indonesia): A coupled offshore-onshore model. Mar Geol 268 (1-4):43-54

Paris R, Lavigne F, Wassmer P, Sartohadi J (2007) Coastal sedimentation associated with the December 26, 2004 tsunami in Lhok Nga, west Banda Aceh (Sumatra, Indonesia). Mar Geol 238 (14):93-106

Paris R, Wassmer P, Sartohadi J, Lavigne F, Barthomeuf B, Desgages E, Grancher D, Baumert P, Vautier F, Brunstein D, Gomez C (2009) Tsunamis as geomorphic crises: Lessons from the December 26, 2004 tsunami in Lhok Nga, West Banda Aceh (Sumatra, Indonesia). Geomo 104 (1-2):59-72

Peters R, Jaffe B, Gelfenbaum G (2007) Distribution and sedimentary characteristics of tsunami deposits along the Cascadia margin of western North America. SedG 200 (3-4):372-386

Piatanesi A, Lorito S (2007) Rupture process of the 2004 Sumatra-Andaman earthquake from tsunami waveform inversion. Bulletin of the Seismological Society of America 97 (1 A SUPPL.):S223-S231

Pinegina TK, Bourgeois J, Bazanova LILI, Melekestsev IV, Braitseva OA (2003) A millennial-scale record of holocene tsunamis on the Kronotskiy Bay coast, Kamchatka, Russia. QuRes 59 (1):36-47

Pritchard D, Dickinson L (2008) Modelling the sedimentary signature of long waves on coasts: implications for tsunami reconstruction. SedG 206 (1-4):42-57

Qiu Q, Huang Z, Megawati K, Sieh K, Natawidjaja DH A scenario study of tsunami-induced inundation for Pariaman, West Sumatra, Indonesia. In: 5th Annual International Workshop & Expro on Sumatra Tsunami Disaster & Recovery 2010, Banda Aceh, Indonesia, 2010.

Roelvink D, Reniers A, Dongeren Av, Vries JvTd, Lescinski J, McCall R (2008) Xbeach model description and manual.

Roelvink D, Reniers A, van Dongeren A, van Thiel de Vries J, McCall R, Lescinski J (2009) Modelling storm impacts on beaches, dunes and barrier islands. Coastal Engineering 56 (11-12):1133-1152

Sato H, Shimamoto T, Tsutsumi A, Kawamoto E (1995) Onshore tsunami deposits caused by the 1993 Southwest Hokkaido and 1983 Japan Sea earthquakes. Pure and Applied Geophysics PAGEOPH 144 (3-4):693-717

Shi S, Dawson AG, Smith DE (1995) Coastal sedimentation associated with the December 12th, 1992 tsunami in Flores, Indonesia. Pure and Applied Geophysics PAGEOPH 144 (3-4):525-536

Simpson G, Castelltort S (2006) Coupled model of surface water flow, sediment transport and morphological evolution. Computers & Geosciences (32):1600–1614. doi:10.1016/j.cageo.2006.02.020

Smith DE, Foster IDL, Long D, Shi S (2007) Reconstructing the pattern and depth of flow onshore in a palaeotsunami from associated deposits. SedG 200 (3-4):362-371

Spiske M, Weiss R, Bahlburg H, Roskosch J, Amijaya H (2010) The TsuSedMod inversion model applied to the deposits of the 2004 Sumatra and 2006 Java tsunami and implications for estimating flow parameters of palaeo-tsunami. SedG 224 (1-4):29-37

Sugawara M, Ohkubo S, Imamura F (2004) Basic study on sand sedimentation by a tsunami on an uniform slope. Tohuku Journal of natural Disaster Science 40:265-270

Switzer AD, Jones BG (2008) Large-scale washover sedimentation in a freshwater lagoon from the southeast Australian coast: Sea-level change, tsunami or exceptionally large storm? Holocene 18 (5):787-803

Takahashi T, Shuto N, Imamura F, Asai D Modeling sediment transport due to tsunamis with exchange rate between bed load layer and suspended load layer. In: Proceedings of the International Conference on Coastal Engineering, ASCE, 2000. pp 1508-1519

Titov VV, Synolakis CE (1998) Numerical modeling of tidal wave runup. J Waterway Port Coast Ocean Eng 124 (4):157-171

Van Rijn LC (1993) Principles of sediment transport in rivers, estuaries and coastal seas. . Aqua Publications, The Netherlands

Wang X (2009) User manual for Cornell multi-grid coupled tsunami model-COMCOT V1.7. . http://ceeserver.cee.cornell.edu/pll-group/doc/COMCOT_User_Manual_v1_7.pdf. Accessed 11 October 2011

Wang X, Liu PLF (2006) An analysis of 2004 Sumatra earthquake fault plane mechanisms and Indian Ocean tsunami. Journal of Hydraulic Research 44 (2):147-154

Wang X, Liu PLF (2007) Numerical simulations of the 2004 Indian Ocean tsunamis-coastal effects. Journal of Earthquake and Tsunami 1 (3):273-297

Weiss R, Bahlburg H (2006) A note on the preservation of offshore tsunami deposits. Journal of Sedimentary Research 76 (11-12):1267-1273

Wijetunge JJ, Wang X, Liu PLF (2008) Indian Ocean tsunami on 26 December 2004: numerical modelling of inundation in three cities on the south coast of Sri Lanka. Journal of Earthquake and Tsunami 2 (2):133-155

Xiao H, Young YL, Prévost JH (2010) Hydro- and morpho-dynamic modeling of breaking solitary waves over a fine sand beach. Part II: Numerical simulation. Mar Geol 269 (3-4):119-131

List of figures

thickness; b): tsunami deposit thickness along the cross-sections A-A and B-B; c): vertical grain size distribution at those specified locations marked by the black triangles in b); d): lateral grain size distribution along the cross-sections A-A and B-B. Equivalent grain size, which is the sum of each grain size times its volume percentage, was used in both c) and d). The distance is measured from the start point of each cross-section.

Fig. 11 The top row shows the initial grain size compositions: (a) for the distribution A; (b) for the distribution B; (c) for the distribution C and (d) for the distribution D. The color bar indicates the volume percentage of 0.2 mm sand; 1 means 100% of 0.2-mm sand and 0 means 0% of 0.2-mm sand. The bottom row shows the grain size compositions in the topmost layer 1 hour after the tsunami attack: (e) for the distribution A; (f) for the distribution B; (g) for the distribution C; (h) for the distribution D .

Fig. 12 Comparison of the simulated deposit thickness with the measured ones for 4 different initial sediment compositions

Fig. 13 Initial surface elevation map derived from 2 different fault models: a) is source model B, which was proposed by Chlieh et al (2007), and the uplift and subsidence are doubled to get tsunami heights comparable with the measured data; b) is for the source model C, which was proposed by Chlieh et al (2007). Source model A is shown in Fig. 3.

Fig. 14 Left: comparison of the simulated tsunami heights with the surveyed data for source models A, B and C; Right: comparison of the simulated tsunami deposit thickness with measured data along the cross-section A-A (top) and for the simulated tsunami deposit thickness along the cross-section B-B (bottom). The distance is measured from the start point of each cross-section.

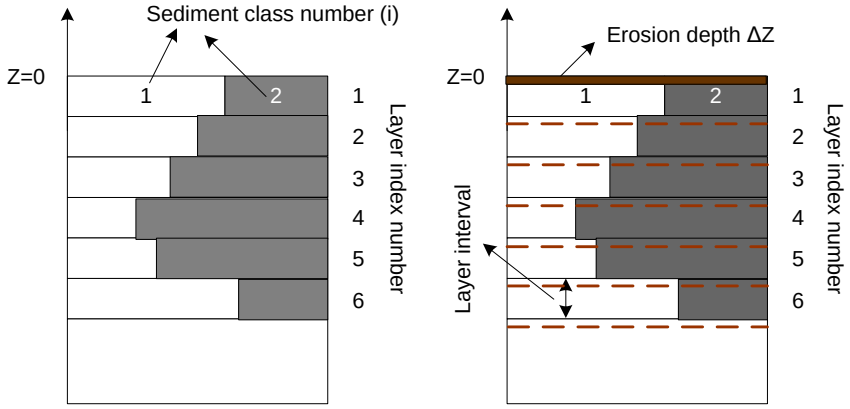

Fig. 1 Sketch of multiple sediment classes in multiple layers, left: initial distribution; right: after erosion (the length of the white or gray color indicates the proportion of each sediment class)

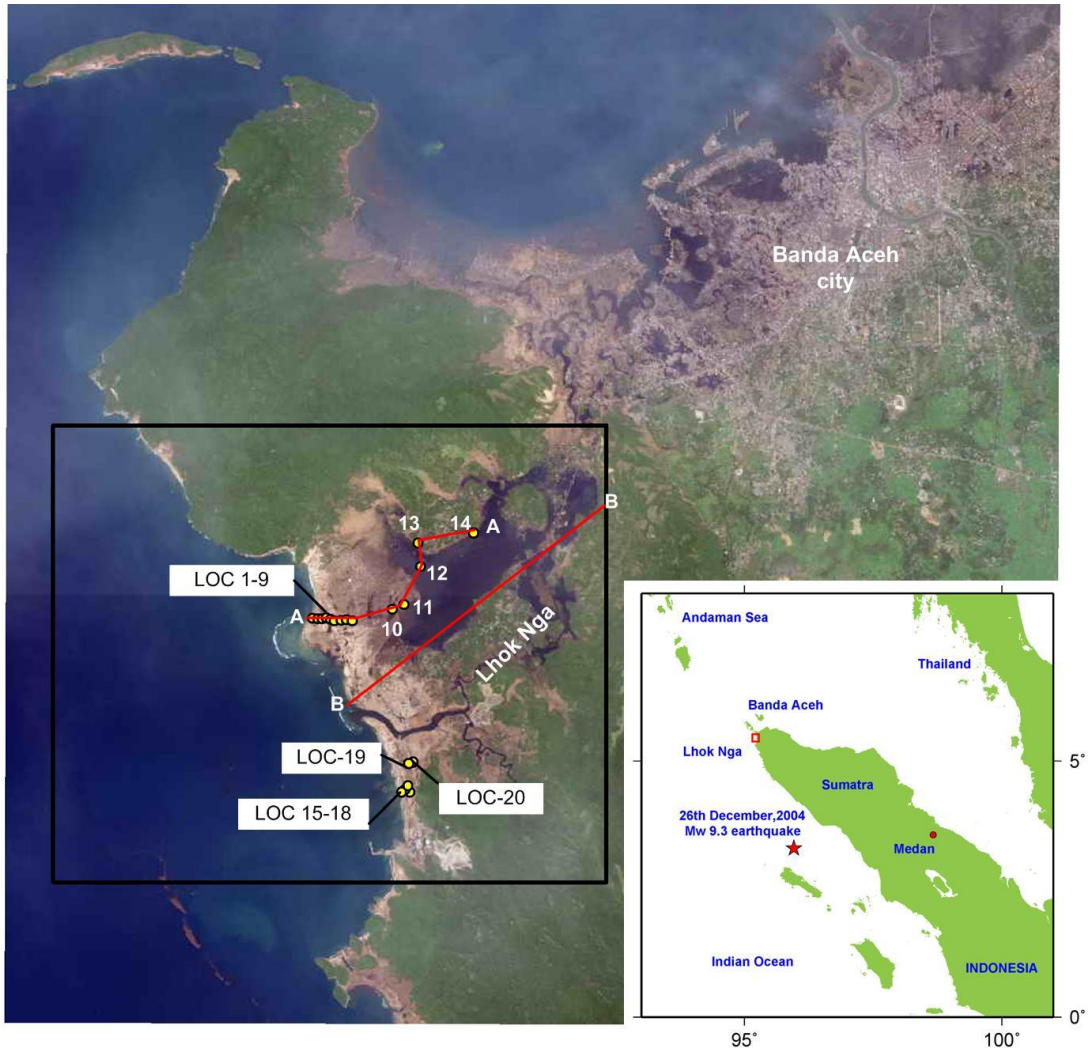

Fig. 2 The map of the Lhok Nga Bay, west coast of Banda Aceh, Indonesia, as shown on the IKONOS satellite image after the 2004 Indian Ocean tsunami: the study area is marked by the black rectangle; yellow dots indicate the locations where tsunami deposit samples were collected.

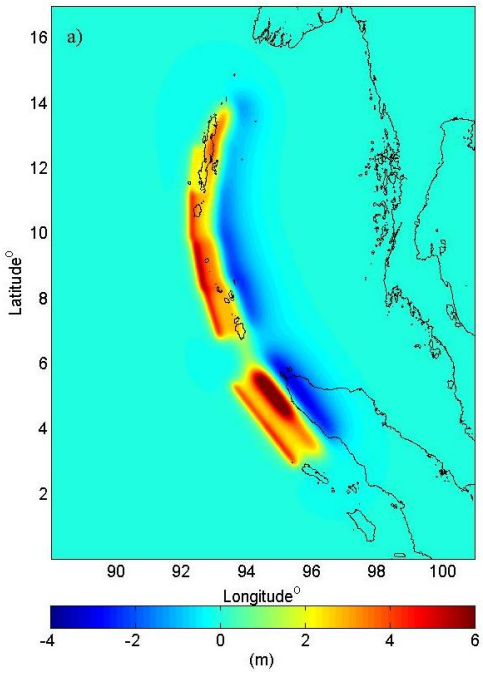

Fig. 3 The map of the initial surface elevation derived from the fault model that was initially proposed by Banerjee et al (2007) and later updated by Piatanesi and Lorito (2007)

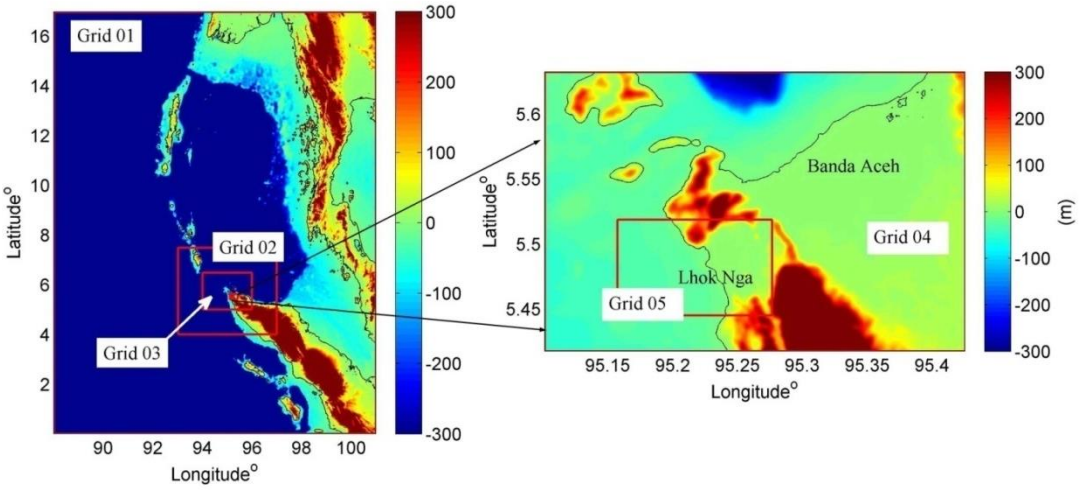

Fig. 4 Nested grids for COMCOT-SED simulation

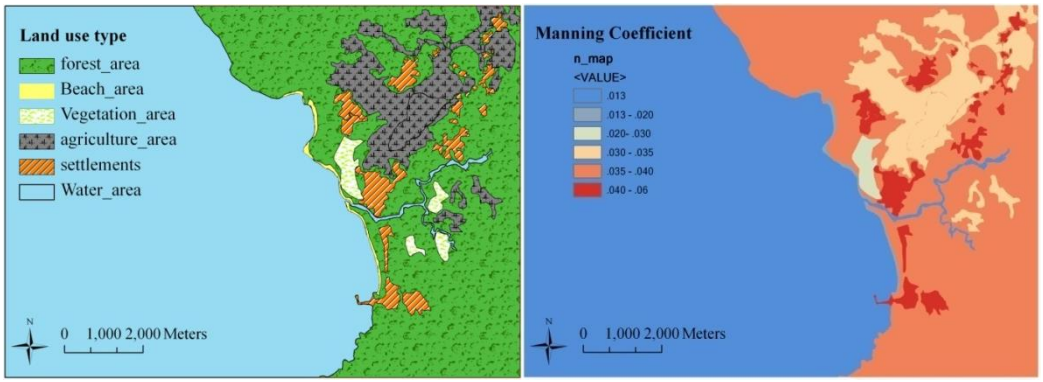

Fig. 5 Left: the classification of land use in Lhok Nga; Right: map of Manning's coefficient

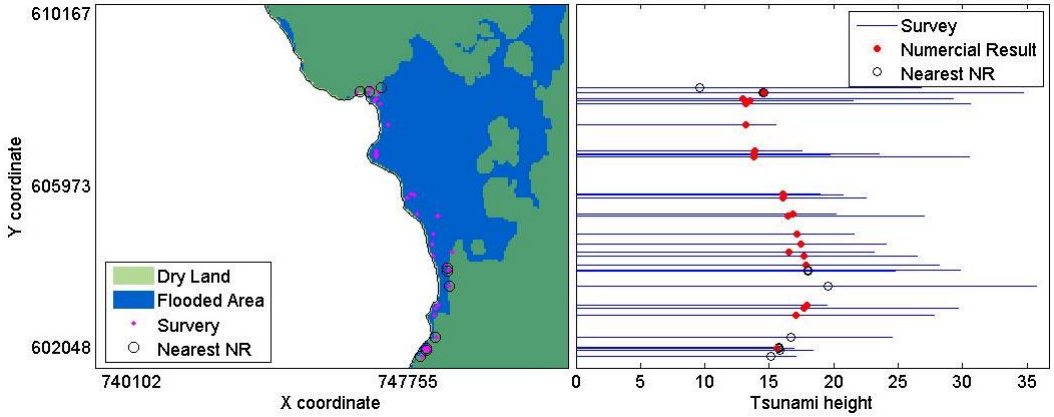

Fig. 6 Inundation map (left) and comparison of the simulated tsunami heights with the measured data (right). In the right panel, the blue bars are for the survey data (locations are marked by red dots in left panel) and the black circles are for the Nearest Numerical Results (Nearest NR) (Several surveyed locations is not flooded in the numerical simulation and thus no tsunami wave heights are predicted at those surveyed locations. However, numerical results for the wave heights closest to these survey locations are reported for reference.)

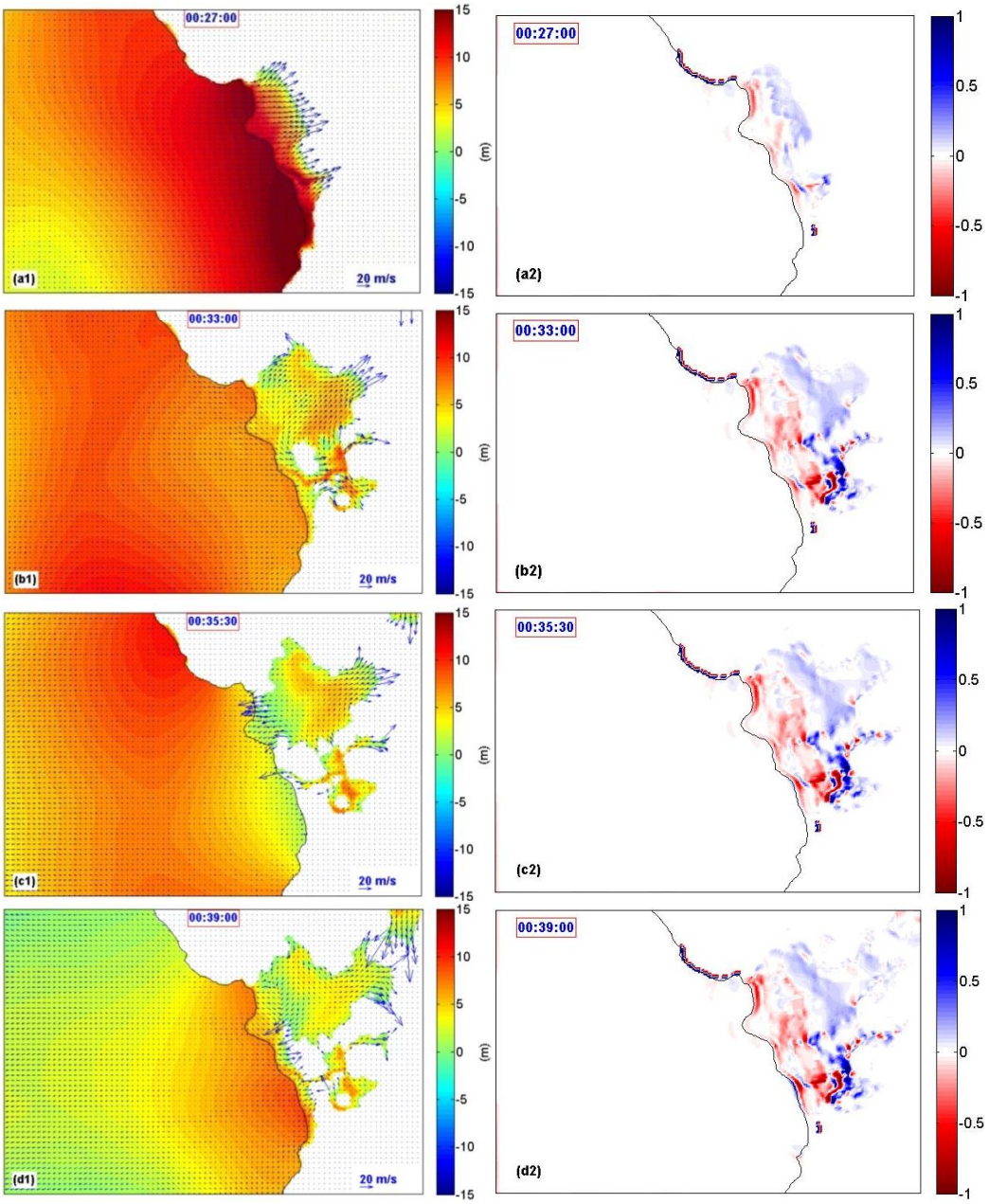

Fig. 7 Snapshots of velocity maps (left) and the corresponding maps for bed-elevation change (right) in the first one hour: (a1) and (a2) at 27 minutes; (b1) and (b2) at 33 minutes; (c1) and (c2) at 35.5 minutes; (d1) and (d2) at 39 minutes.

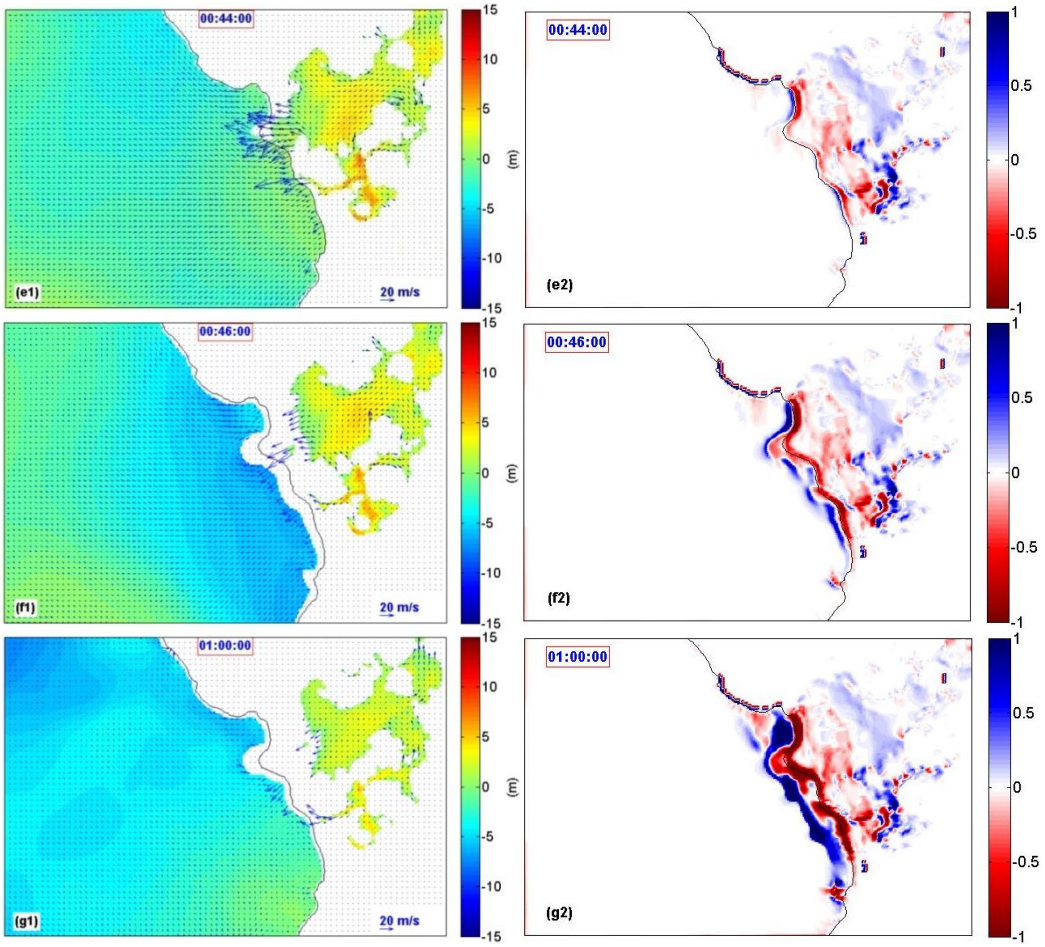

Fig. 7 (continued). Snapshots of velocity maps (left) and the corresponding maps for bed-elevation change (right) in the first one hour: (e1) and (e2) at 44 minutes; (f1) and (f2) and 46 minutes; (g1) and (g2) at 1 hour.

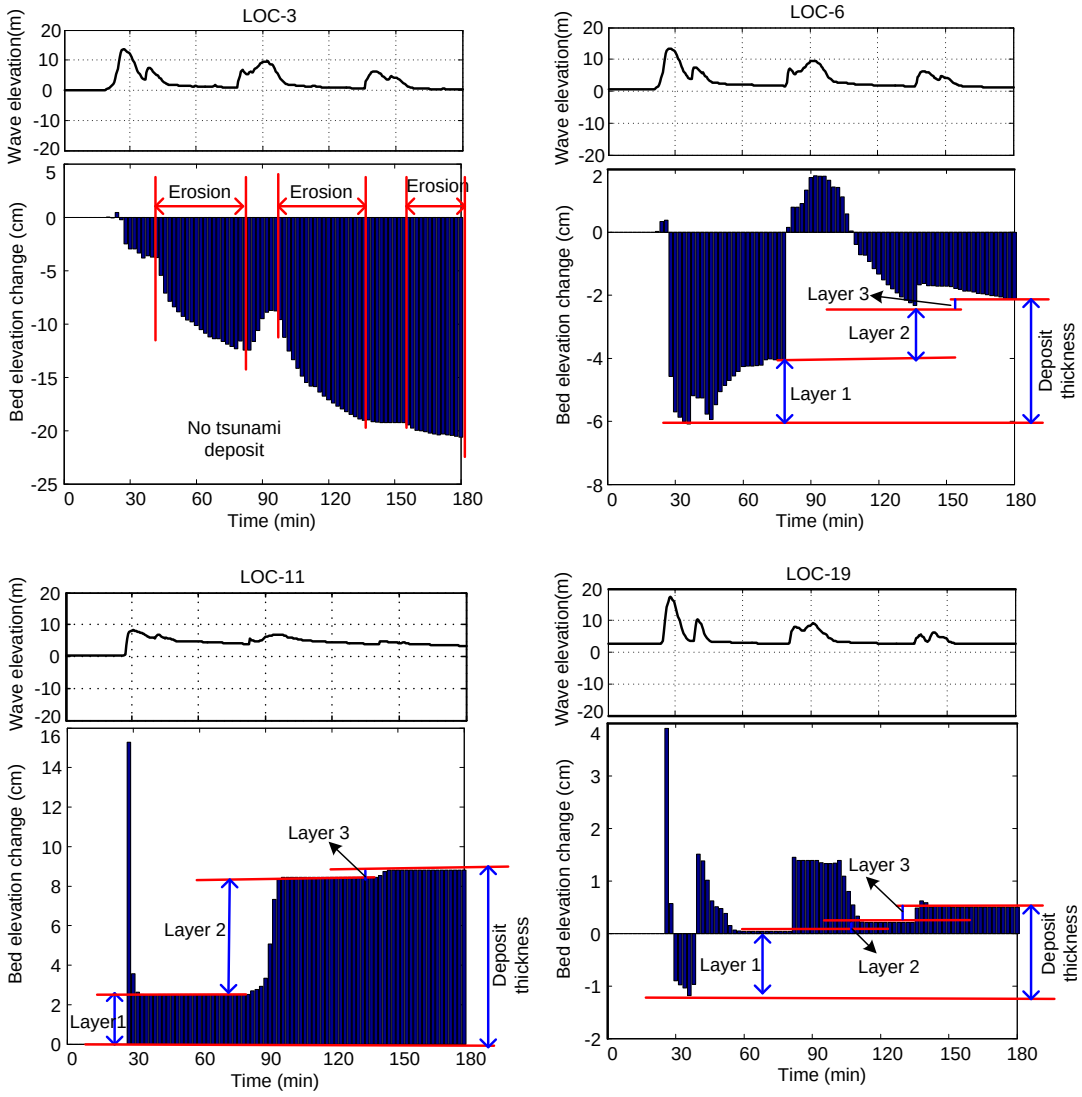

Fig. 8 Time series of the bed elevation changes at 4 typical surveyed locations

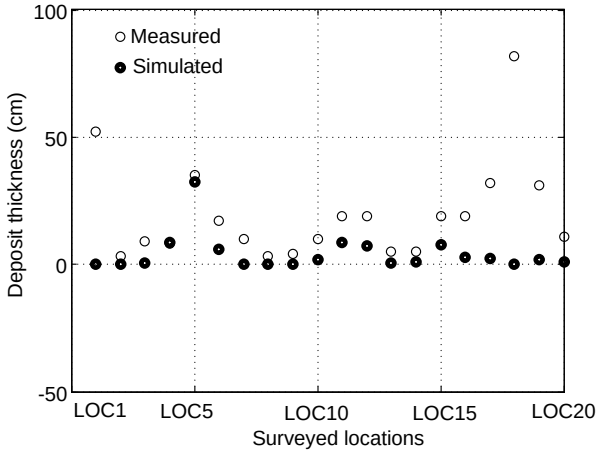

Fig. 9 Comparison of the simulated tsunami-deposit thickness with the measured data

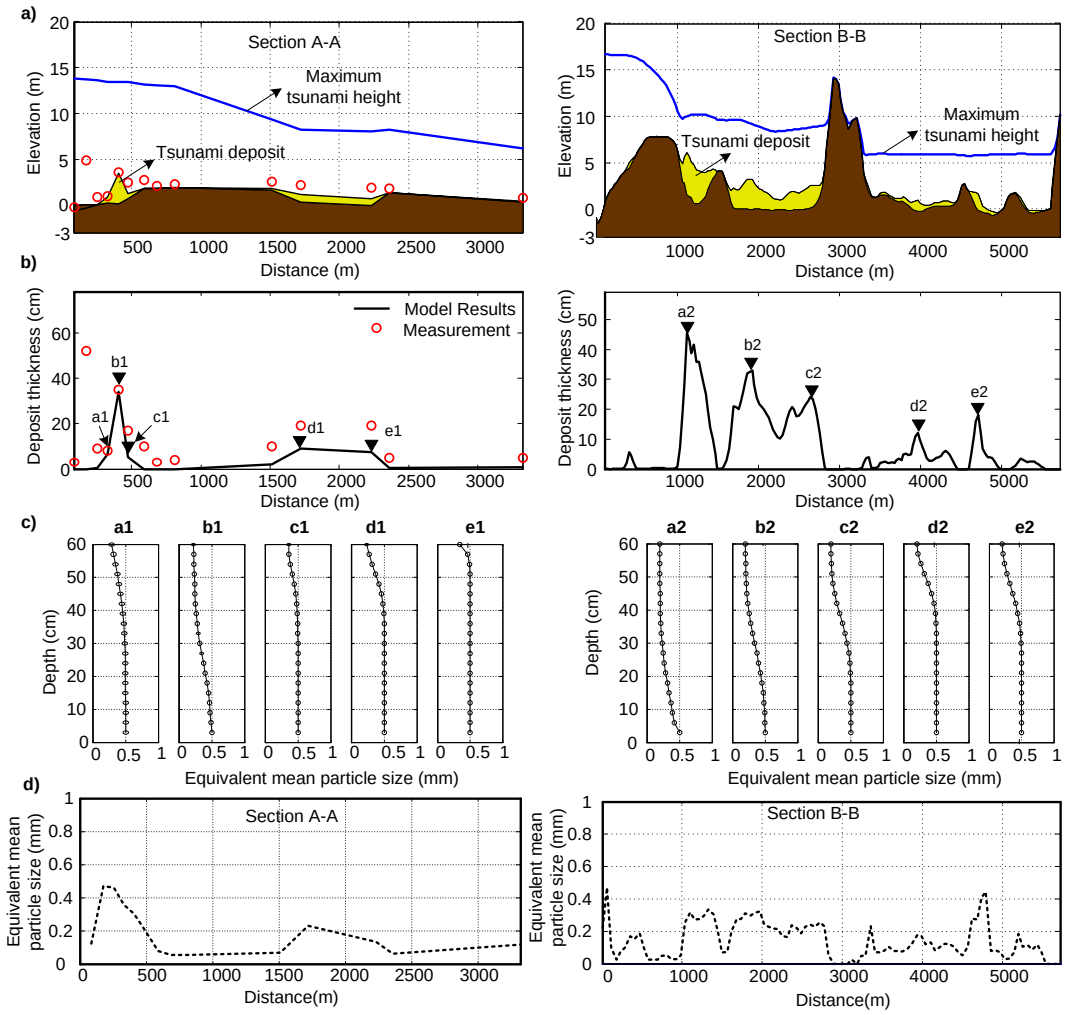

Fig. 10 Spatial distribution of tsunami deposits. a): topographic profile, maximum tsunami height and tsunami deposits along the cross-section A-A (measured profile) and the cross-section B-B (shown in Fig. 2). A 10 times vertical exaggeration is applied on the tsunami deposit thickness; b): tsunami deposit thickness along the cross-sections A-A and B-B; c): vertical grain size distribution at those specified locations marked by the black triangles in b); d): lateral grain size distribution along the cross-sections A-A and B-B. Equivalent grain size, which is the sum of each grain size times its volume percentage, was used in both c) and d). The distance is measured from the start point of each cross-section.

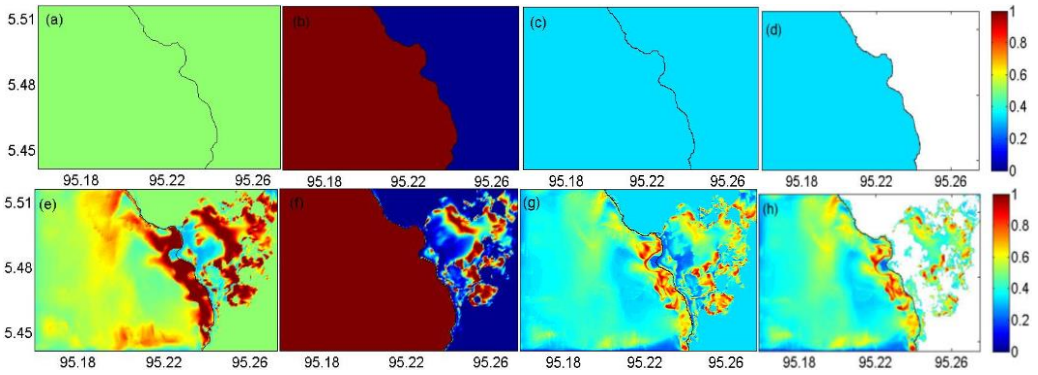

Fig. 11 The top row shows the initial grain size compositions: (a) for the distribution DA; (b) for the distribution DB; (c) for the distribution DC and (d) for the distribution DD. The color bar indicates the volume percentage of 0.2 mm sand; 1 means 100% of 0.2-mm sand and 0 means 0% of 0.2-mm sand. The bottom row shows the grain size compositions in the topmost layer 1 hour after the tsunami attack: (e) for the distribution DA; (f) for the distribution DB; (g) for the distribution DC; (h) for the distribution DD.

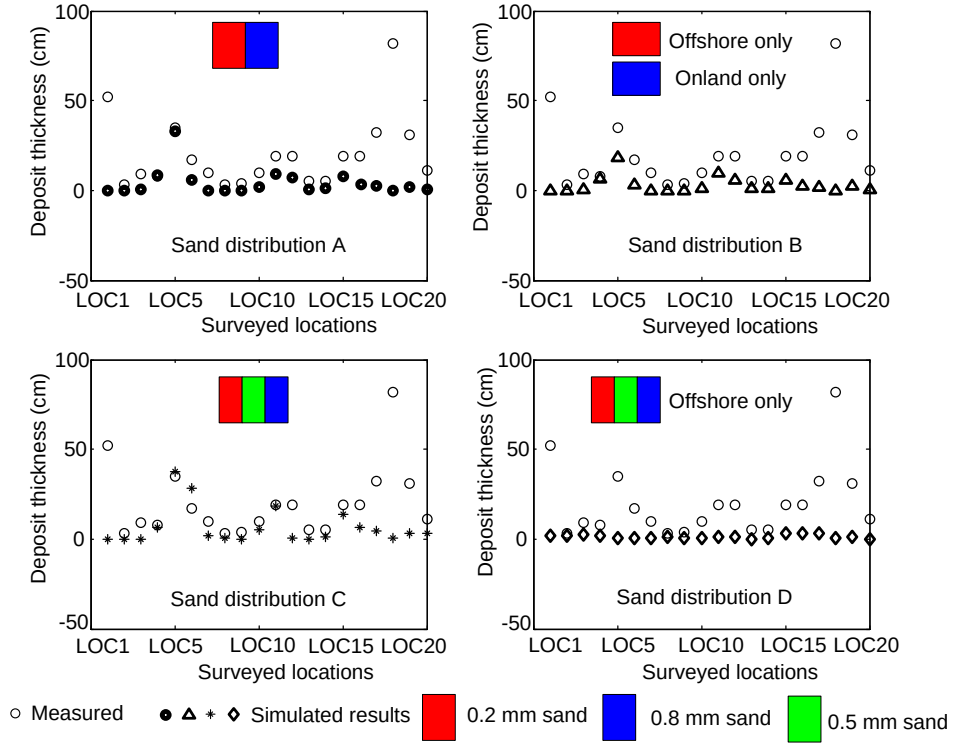

Fig. 12 Comparison of the simulated deposit thickness with the measured ones for 4 different initial sediment compositions

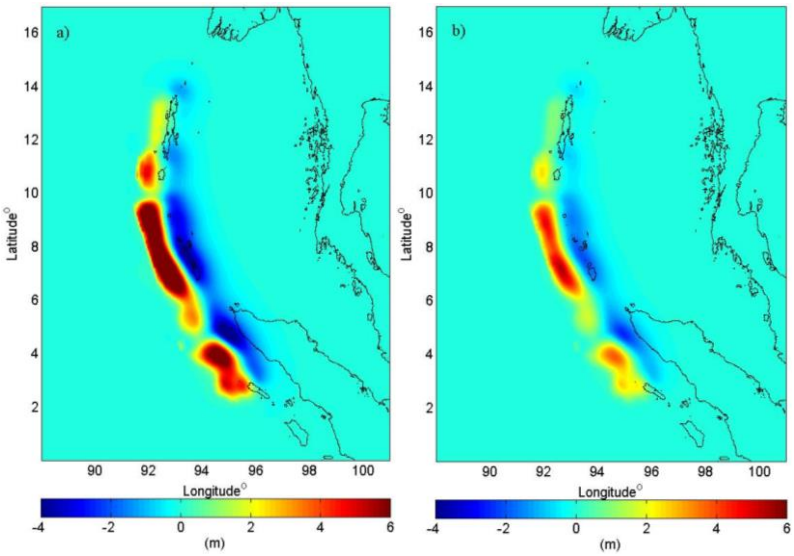

Fig. 13 Initial surface elevation map derived from 2 different fault models: a) is source model B, which was proposed by Chlieh et al (2007), and the uplift and subsidence are doubled to get tsunami heights comparable with the measured data; b) is for the source model C, which was proposed by Chlieh et al (2007). Source model A is shown in Fig. 3.

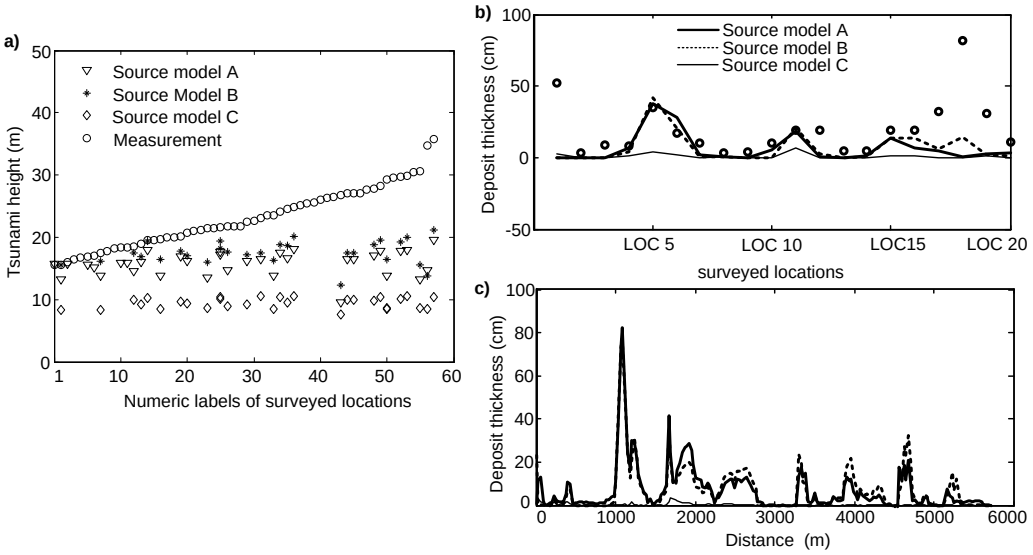

Fig. 14 Left: comparison of the simulated tsunami heights with the surveyed data for source models A, B and C; Right: comparison of the simulated tsunami deposit thickness with measured data along the cross-section A-A (top) and for the simulated tsunami deposit thickness along the cross-section B-B (bottom). The distance is measured from the start point of each cross-section.

List of tables

Table 1 Information on the setup of the five grids for COMCOT-SED simualtions

	Grid 01	Grid 02	Grid 03	Grid 04	Grid 05
Number of grids	743 ×971	684 × 597	1026 ×768	501 × 333	736 ×456
Lati. (degree)	88 E ~101 E	93 E ~ 97 E	94 E ~ 96 E	95.1 E ~ 95.42 E	95.16 E~ 95.27 E
Longi. (degree)	0 ~ 17 N	4.0 N ~ 7.5 N	5 N ~ 6.5 N	5.42 N ~ 5.63 N	5.44 N ~ 5.51 N
Grid size (m)	1944	648	216	72	18
Parent grid	(None)	Grid 01	Grid 02	Grid 03	Grid 04
Grid size ratio	(None)	3	3	3	4
Time step (in sec)	0.01	0.01	0.01	0.01	0.01
Coordinate system	Spherical	Spherical	Spherical	Cartesian	Cartesian
SWE	Linear	Linear	Linear	Nonlinear	Nonlinear

Table 2 Volume percentage of each grain size in four different initial sand distributions

Sand distribution	Offshore region			Onshore region		
	0.2 mm	0.5 mm	0.8 mm	0.2 mm	0.5 mm	0.8 mm
DA	50%	0%	50%	50%	0%	50%
DB	100%	0%	0%	0%	0%	100%
DC	33.33%	33.33%	33.33%	33.33%	33.33%	33.33%
DD	33.33%	33.33%	33.33%	0%	0%	0%